

# Enhanced Plasmonic Hot-Carrier Transfer in Au/WS<sub>2</sub> Heterojunctions under Nonequilibrium Condition

Xinglin Wen,\* Sijie Chen, Jiaxin Zhao, Wei Du,\* and Weijie Zhao\*

Cite This: *ACS Photonics* 2022, 9, 1522–1528

Read Online

ACCESS |



Metrics &amp; More



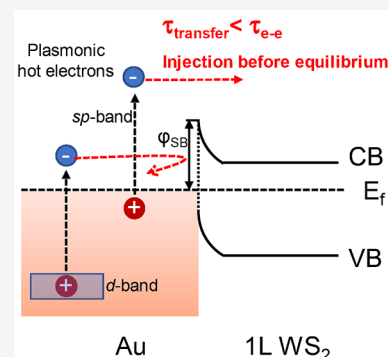
Article Recommendations



Supporting Information

**ABSTRACT:** The plasmonic hot-carrier is of great importance in applications of photon harvesting, photocatalysis, and photodetectors. However, the plasmonic hot-carrier harvesting efficiency is limited by their ultrafast thermalization in plasmonic nanostructures. Here, we revealed that the hot-carrier of the gold nanostructure could be captured by monolayer-WS<sub>2</sub> before thermalization to enhance the harvesting efficiency. We found that the thermalization time of electrons within intraband transition was as long as 600 fs under pump fluence of 21  $\mu\text{J}/\text{cm}^2$ , which was much longer than the charge transfer time of 160 fs, and thus nonthermal electrons could be transferred prior to thermalization. We further demonstrated that the contribution of nonthermal electrons increased with decreasing pump fluence or increasing lattice temperature. Finally, the decay process of plasmonic hot-carrier transferred into WS<sub>2</sub> was strikingly different from that of intrinsic carriers in WS<sub>2</sub> via direct photoexcitation, which is attributed to their different recombination channels. Our results provide insights for microscopic understanding of the nonequilibrium carrier-transfer physics and will facilitate performance optimization of plasmonic hot-carrier-based optoelectronic devices.

**KEYWORDS:** plasmonic, hot carriers, 2D materials, nonequilibrium, transient absorption



Localized Surface Plasmon Resonance (LSPR), namely, collective oscillations of conductive electrons in metallic nanostructure with subwavelength dimension, has attracted substantial attention due to the ability to enhance and confine near-fields.<sup>1–3</sup> The confined near-fields, termed “hot-spots”, can serve as an amplifier to enhance absorption, scattering, and photoluminescence of various materials and thus provide an essential way to control the light–matter interaction. For instance, it is widely applied in surface-enhanced Raman scattering,<sup>4–6</sup> surface-enhanced infrared absorption,<sup>7,8</sup> plasmonic nanolasers,<sup>9–11</sup> strong light–matter coupling system,<sup>12–15</sup> and so on.

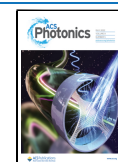
Apart from enhancing light–matter interaction, hot carriers can be generated from nonradiative decay of surface plasmons and bear great potential for device applications.<sup>16–19</sup> The generation rate of a plasmonic hot carrier is significantly increased at the plasmon resonance due to the intensified absorption cross section.<sup>20</sup> In addition, a plasmonic hot-carrier with large kinetic energy could overcome the potential barrier and transfer to semiconductors in well-designed heterojunctions.<sup>21–24</sup> The generation and transfer process of the plasmonic hot carrier occurs on an ultrafast time scale ranging from tens of femtoseconds to a few picoseconds.<sup>16,19,20,25</sup> These intriguing properties render the plasmonic hot-carrier promising in the applications of photocatalysis,<sup>26,27</sup> photodetection,<sup>22,28–30</sup> ultrafast optical switches, and modulators.<sup>31–33</sup>

For the plasmonic hot-carrier based devices, substances (usually molecules or semiconductors) which are in contact

with the metallic nanostructure can capture the plasmonic hot-carrier to realize novel functionalities. For example, plasmonic hot-electrons transferred into molecules adsorbed on the metal surface were utilized to catalyze chemical reactions. In addition, the efficient hot-electron injection holds great potential for the development of superior photovoltaic and photodetector devices.<sup>34,35</sup> In particular, for the metal/semiconductor heterostructures in photovoltaic and photodetector devices, it is desirable to understand the dynamic behavior of the plasmonic hot-carrier and further optimize the performance of corresponding devices. In general, we can decipher the dynamics of the plasmonic hot-carrier into three steps in sequence: (i) the nonradiative decay of surface plasmon can generate a hot-carrier via interband or intraband transition, (ii) nonequilibrium electrons thermalize rapidly (tens of femtoseconds) by the electron–electron (e–e) scattering, (iii) the thermalized electrons transfer their energy to lattice by electron–phonon (e–p) interaction or injected to nearby semiconductors.<sup>19,20,23–25,36–39</sup> Usually, the e–e lifetime  $\tau_{e-e}$  (tens of femtoseconds) is much shorter than the e–p lifetime  $\tau_{e-p}$  (few picoseconds). Therefore, it can be assumed

Received: December 16, 2021

Published: April 25, 2022



that the generated electrons thermalize instantly, and the carrier dynamics could be fully described by the lattice temperature ( $T_l$ ) and effective electron temperature ( $T_e$ ), namely, the two-temperature model (TTM).<sup>40</sup> However,  $\tau_{e-e}$  is not always that short under certain circumstances, such as at low excitation power, and thus the contribution of nonthermal electrons is not negligible.<sup>18,41,42</sup> The ultrafast laser-induced nonequilibrium states can provide various novel functionalities that cannot be accessed by thermalized states as discussed in this very recent review.<sup>43</sup> Indeed, recent reports show that hot-electrons of graphene<sup>44</sup> and FICO nanocrystals<sup>45</sup> could be captured before completion of thermalization and give rise to a much higher electron harvesting efficiency. It is thus highly desired to gain a fundamental understanding of how nonthermal electrons influence the hot-carrier injection process at the plasmonic structure/semiconductors interface.

Herein, we fabricate heterojunctions consisting of a gold (Au) plasmonic nanodisk array and monolayer (1L) WS<sub>2</sub>. The ultrafast dynamics of hot-electrons and their transfer process in these heterojunctions are investigated by employing transient absorption (TA) spectroscopy. The  $\tau_{e-e}$  is found to be  $\sim 600$  fs and  $\sim 100$  fs for the intraband transition at 725 nm and interband transition at 520 nm, respectively. We further demonstrate that the contribution of nonthermal electrons from intraband transitions can significantly enhance the charge transfer efficiency, which is evidenced by the enlarged TA signal of the A excitons of WS<sub>2</sub>. We also find that the higher lattice temperature not only enhances transfer efficiency but also reduces the charge transfer time scale. Finally, the decay dynamics of hot-electrons after transferring to 1L WS<sub>2</sub> is quite different from that of intrinsic electrons directly excited with a 420 nm laser, because the hot-carrier can recombine at the interface rapidly.

## RESULTS

1L WS<sub>2</sub> is grown on sapphire substrate with chemical vapor deposition (CVD) methods as shown in Figure 1a (white

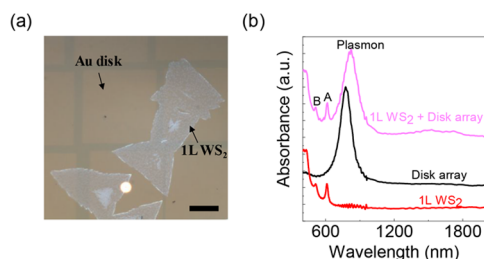


**Figure 1.** Sample characterization. (a) Optical image of the monolayer WS<sub>2</sub>/Au disk array heterojunctions on sapphire. Au disks are fabricated directly on top of WS<sub>2</sub>. The scale bar is 20  $\mu\text{m}$ . (b) Absorbance of the pristine 1L WS<sub>2</sub> (red), bare Au disk array (black), and Au/WS<sub>2</sub> heterojunctions (magenta). A and B denote the A and B exciton, respectively.

flakes). Subsequently, a PMMA layer is spin-coated on as-prepared samples, and electron beam lithography (EBL) is utilized to fabricate the disk array patterns followed by the metal deposition and lift-off procedures as shown in Figure 1a (yellow squares). During the EBL process, an E-spacer is used to eliminate the charge effect arising from the insulating property of sapphire (see details in Methods). The diameter of the Au disks is 100 nm, and the periodicity is 200 nm. The

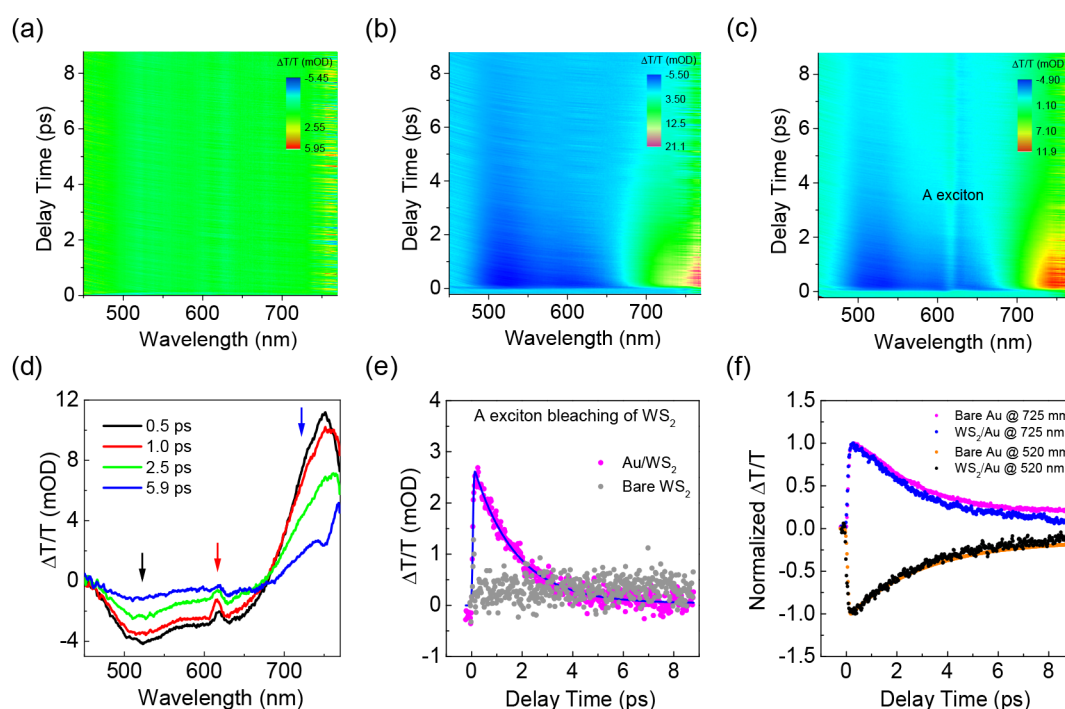
optical image of the Au disk array and 1L WS<sub>2</sub> heterojunctions are shown in Figure 1a.

Pristine 1L WS<sub>2</sub> exhibits two absorption peaks at 612 and 512 nm, which correspond to A and B excitons, respectively<sup>46</sup> (red curve in Figure 1b). A and B excitons originate from the transition between the split valence band to the conduction band as a result of spin–orbit coupling.<sup>47</sup> Plasmon resonance at 780 nm is observed for the bare Au disk array on sapphire as shown in the black curve in Figure 1b. For the absorption spectrum of the Au/WS<sub>2</sub> hybridized structure as shown by the magenta curve in Figure 1b, A and B exciton resonances remain at the same position as those of pristine 1L WS<sub>2</sub>, while the plasmon resonance of the Au disk red-shifts to  $\sim 820$  nm. The red-shift of plasmon resonance is attributed to the larger refractive index of 1L WS<sub>2</sub> ( $n \sim 3.5$  @ 780 nm)<sup>48</sup> compared with sapphire ( $n \sim 1.76$ ). Based on the resonance wavelength of excitons and plasmon, we can use lasers at a proper wavelength to excite the plasmon resonance but not the excitonic transition in 1L WS<sub>2</sub> in order to investigate nonequilibrium hot-carrier dynamics.

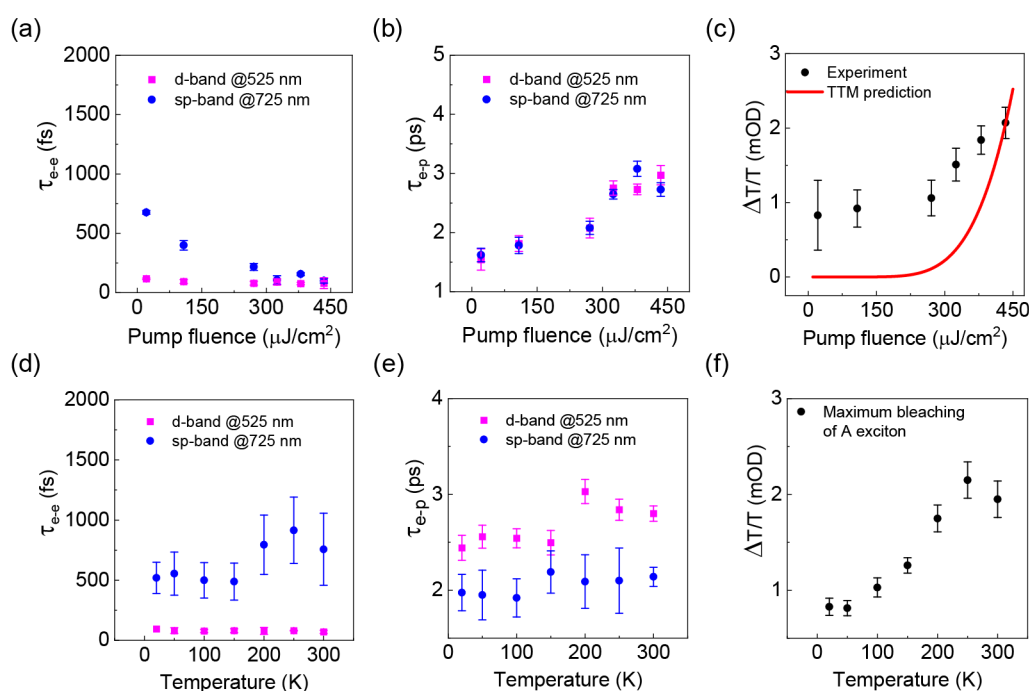
TA spectroscopy is a well-established method to study the ultrafast dynamics of nonthermal electrons in metal/semiconductor heterojunctions. The pulse width and repetition rate of the pump/probe laser are  $\sim 100$  fs and 1 kHz, respectively. The broadband probe beam with wavelength ranging from 400 to 780 nm is generated with a CaF<sub>2</sub> crystal. We choose the 820 nm pump laser for two reasons: (i) it can generate plasmonic hot-carrier efficiently as it resonates with the plasmon resonance of Au disks; (ii) its photon energy is much lower than that of A excitons of 1L WS<sub>2</sub>, which can avoid the direct excitation of A excitons through photoabsorption.

Figure 2a shows the TA contour map of pristine 1L WS<sub>2</sub> excited with 820 nm excitation laser at a pump fluence of 60  $\mu\text{J}/\text{cm}^2$ , and no TA signal can be observed due to its negligible absorption at 820 nm. At the same time, we can also exclude two-photon absorption (TPA) of 1L WS<sub>2</sub> at the corresponding pump wavelength and fluence. In contrast, ground-state bleaching (GSB) of A and B excitons can be observed with the 420 nm pump laser because of the efficient single-photon absorption of 1L WS<sub>2</sub> (Figure S1, Supporting Information). Furthermore, TA spectra of the bare Au disk array is measured under the same condition as shown in Figure 2b; broad GSB and photon induced absorption (PIA) are observed around 800 and 520 nm, which are attributed to the intraband (sp-band) transition and interband (d-band) transition induced by nonradiative surface plasmon decay, respectively. The broad negative  $\Delta T/T$  is due to a plasmon absorption frequency shift and spectra broadening, which leads to negative wings near the surface plasmon wavelength.<sup>49–51</sup>

TA spectra of Au/WS<sub>2</sub> heterojunctions in Figure 2c indicate a GSB signal at 612 nm, which is assigned to A exciton of 1L WS<sub>2</sub>. By comparing the results in Figure 2a and 2c, we can conclude that the appearance of GSB at the A exciton resonance originated from the plasmonic hot-electron injection into WS<sub>2</sub>. At first, hot electrons are produced with nonradiative decay of the surface plasmon under 820 nm excitation and they have sufficient energy to overcome the Schottky barrier to be injected to WS<sub>2</sub>. Electrons injected to the conduction band of WS<sub>2</sub> cause the exciton bleaching signal  $\Delta T/T$  (Figure S2). Several TA spectra at various delay times shown in Figure 2d reveal evident TA signal of the A exciton (red arrow), d-band (black arrow), and sp-band (blue arrow) transitions. Figure 2e shows the kinetics of the A exciton at 612 nm for the pristine



**Figure 2.** Ultrafast carrier dynamics in Au disk, 1L WS<sub>2</sub>, and their heterojunctions. TA spectra of (a) pristine 1L WS<sub>2</sub>, (b) bare Au disk array, and (c) Au array/1L WS<sub>2</sub> heterojunctions under 820 nm pump at 300 K. (d) TA spectra of Au array/1L WS<sub>2</sub> at different delay times. (e) Exciton kinetics at 612 nm of pristine 1L WS<sub>2</sub> and Au/WS<sub>2</sub> sample under 820 nm pump. (f) Kinetics of bare Au and Au/WS<sub>2</sub> sample at interband transition (520 nm) and intraband transition (725 nm), respectively.



**Figure 3.** Pump fluence- and temperature-dependent dynamics of hot-carrier. (a) Electron–electron and (b) electron–phonon lifetime at 525 and 725 nm of Au array/1L WS<sub>2</sub> heterojunctions, respectively, as a function of pump fluence. (c) Maximum GSB magnitude of A exciton of 1L WS<sub>2</sub> in the hybridized structure at various fluences. The red curve is the simulation result by using the two-temperature model (TTM). Temperature-dependent (d) electron–electron and (e) electron–phonon lifetime at 525 and 725 nm as a function of temperature, respectively. (f) Maximum GSB magnitude of A exciton of 1L WS<sub>2</sub> in the hybridized structure at various temperature. The pump fluence is fixed at  $\sim 21 \mu\text{J}/\text{cm}^2$  in (d–f).

WS<sub>2</sub> (gray dots) and Au/WS<sub>2</sub> (magenta dots) under 820 nm excitation, and no TA signal is observed for pristine WS<sub>2</sub> with such a sub-bandgap pump. Because Au nanostructures can

confine the near-field and enhance the absorption coefficient, consequently, TPA may occur in the Au/WS<sub>2</sub> hybrid structure to induce A exciton bleaching. However, we did not see any



steady-state PL under 820 nm femtosecond laser illumination with fluence of 400  $\mu\text{J}/\text{cm}^2$  in Figure S3, excluding the TPA effect. The traces of the sp-band transition at 725 nm and d-band transition at 525 nm of bare Au disks and Au/WS<sub>2</sub> are displayed in Figure 2f. The interpretation of negative  $\Delta T/T$  at 520 nm is that the sp-band transition due to surface plasmon resonance (820 nm) lifts electrons above the Fermi level, and thus increase the d-band absorption.<sup>45,51,52</sup>

For electrons from both d-band and sp-band transitions, their lifetime in Au/WS<sub>2</sub> heterojunctions is shorter than that of bare Au. For instance, it can be observed that  $\tau_{e-e}$  of Au/WS<sub>2</sub> (0.60 ps) is smaller than that of bare Au (0.74 ps) at 725 nm. This is because the presence of WS<sub>2</sub> adds an extra decay channel for the hot electrons of bare Au. The shorter  $\tau_{e-e}$  of Au/WS<sub>2</sub> also indicates that WS<sub>2</sub> can capture hot electrons before their thermalization.

In order to investigate the microscopic process of hot-carrier injection in Au/WS<sub>2</sub> heterojunctions, we conducted TA experiments against pump fluence (21–435  $\mu\text{J}/\text{cm}^2$ ) and lattice temperature (20–300 K). In Figure 3a–c, the nonthermal e–e and thermal e–p interactions are resolved with a biexponential fitting by considering the rise and decay part of TA traces at 525 and 725 nm, respectively.<sup>40,45</sup> Figure 3a shows that the extracted  $\tau_{e-e}$  of sp-band transition ( $\sim 600$  fs) is much larger than that of d-band transition ( $\sim 90$  fs) under low pump fluence. The d-band transitions generate hot electrons occupying states close to the Fermi level which are thermalized rapidly owing to the efficient e–e scattering. On the other hand, electrons from the sp-band transitions are excited to states with energy much higher than Fermi level, which exhibits a reduced scattering rate and thus leads to a larger  $\tau_{e-e}$ . In addition, Figure 3a indicates that  $\tau_{e-e}$  of the sp-band transition decreases gradually with increased pump fluence, while  $\tau_{e-e}$  of d-band transition largely remains unchanged. The higher pump fluence leads to shorter rise time ( $\tau_{e-p}$ ) for two reasons, namely, requiring fewer e–e collisions to raise the temperature of the background of thermal carriers and a larger e–e collision rate because of increased phase space at higher fluence.<sup>53</sup> Figure 3b indicates the  $\tau_{e-p}$  increase from 1 to 3 ps for both transitions with increased pump fluence, which is consistent with previous reports.<sup>54,55</sup> Considering that electron heat capacity is proportional to electron temperature with  $C_e(T_e) = \gamma T_e$ , while the electron–phonon coupling constant ( $G$ ) is independent of  $T_e$ ,<sup>56,57</sup> so that  $\tau_{e-e} = \gamma T_e / G$  increases with pump fluence as Figure 3b shows.

The magnitude of the GSB signal of A excitons ( $\Delta T/T$ ) is proportional to the population of electrons injected into WS<sub>2</sub>, which allows us to estimate the charge transfer efficiency. In Figure 3c, the black dots represent the measured magnitude of the GSB signal of A excitons at varying pump fluence, and the red line represents the theoretically predicted data based on a two-temperature model (Note 1, Supporting Information). Our experimental results are strikingly different from the two-temperature model in which hot electrons are assumed to be thermalized completely before transfer. Such a deviation becomes larger at low pump fluence and is thus attributed to a significant contribution of nonthermal electrons from sp-band transitions. First, a hot-electron from an sp-band transition at sufficiently high energy level can overcome the Schottky barrier at the Au/WS<sub>2</sub> interface and transfer into WS<sub>2</sub>. Second, the thermalization lifetime ( $\sim 600$  fs) of the sp-band hot-electron at low pump fluence is much larger than the

charge-transfer time across the Au/WS<sub>2</sub> interface ( $\sim 160$  fs, will be discussed in Figure 4a) and consequently can transfer

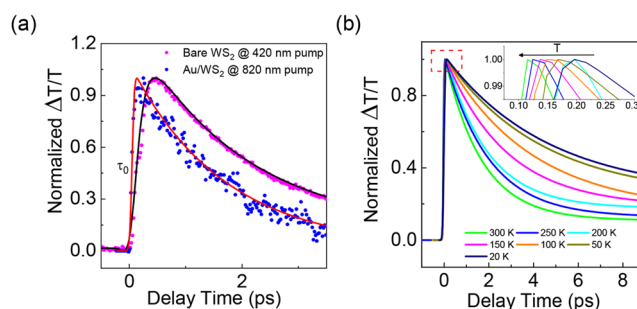


**Figure 4.** Carrier dynamics in 1L WS<sub>2</sub> injected with plasmonic hot-carrier and direct optical excitation. (a) TA kinetics of A exciton bleaching of pristine 1L WS<sub>2</sub> under 420 nm pump (magenta dots) and Au/1L WS<sub>2</sub> sample under 820 nm pump (blue dots) at 300 K. Black and red lines are the corresponding fitting curves. (b) Normalized fitted kinetics for Au/1L WS<sub>2</sub> sample at different temperature. The inset is the zoom-in area indicated with the red dashed square, showing that the TA signal reaches maximum faster at higher temperatures.

before e–e scattering. The e–e scattering rate depends on electron temperature  $T_e$  (namely, pump fluence) with

$$\gamma_{e-e}(T_e) = \frac{\sqrt{3} \pi^4 k_B^2 \omega_p}{256 E_F^2} T_e^2, \text{ where } \omega_p \text{ is the plasma frequency.}$$

It can be seen that lower fluence will have much smaller  $\gamma_{e-e}$ , which means that it will take longer time ( $1/\gamma_{e-e}$ ) to undergo the first e–e collision, making electrons retain their original energy for a longer time for more efficient injection. That is to say, with increased pump fluence, the shortened  $\tau_{e-e}$  leads to a reduced contribution of nonthermal electrons in the electron transfer process. The sudden change of  $\Delta T/T$  at  $\sim 300$   $\mu\text{J}/\text{cm}^2$  is probably related to the nonlinear dependence of  $\tau_{e-e}$  on pump fluence as shown in Figure 3a. It is noteworthy that the heating effect due to laser illumination is negligible, because there is no redshift of A exciton of 1L WS<sub>2</sub> (Figure S4).

Furthermore, the charge transfer efficiency in Au/WS<sub>2</sub> heterojunctions shows temperature dependency. In Figure 3d, we show that the  $\tau_{e-e}$  of the sp-band transition (blue dots) is around  $\sim 600$  fs which is longer than  $\sim 90$  fs of the d-band (magenta square) transition in Figure 3a. When the temperature increases from 20 to 300 K, the  $\tau_{e-e}$  of the sp-band hot-electron increases from  $\sim 600$  to 900 fs in Figure 3d. This behavior can be explained by the nonequilibrium model in which e–e and e–p interactions occur simultaneously but not in a certain sequence. In this case, e–p interactions have an influence on e–e interactions and  $\tau_{e-e}$  has a similar trend to  $\gamma T_{\text{eff}} / G_{\text{eff}}$  where  $T_{\text{eff}}$  and  $G_{\text{eff}}$  are effective temperature and e–p coupling strength.<sup>41,52,58</sup> Our observation is consistent with previous reports.<sup>41</sup> As aforementioned, the incomplete thermalization of electrons (larger  $\tau_{e-e}$ ) will reduce the e–p energy relaxation rate. Consequently, the  $\tau_{e-p}$  should increase with increasing temperature. Indeed, the  $\tau_{e-p}$  of the sp-band transition is observed to increase from 1.97 to 2.14 ps as shown in Figure 3e. We also note that the  $\tau_{e-p}$  of the d-band transition (magenta in Figure 3e) also increases from 2.4 to 2.8 ps, which could be described by the conventional two-temperature model without considering the nonthermal effects, i.e.,  $\tau_{e-p} = \frac{\gamma(T_i + T_e)}{G}$ , where  $\gamma$ ,  $G$ , and  $T_e$  are constant at a fixed pump fluence.<sup>41,42,56</sup> The  $\tau_{e-p}$  is thus proportional to the lattice

temperature  $T_l$ . It is worth noting that the increase of  $\tau_{e-p}$  is small when the lattice temperature increases from 20 to 300 K. This is because the electron temperature is much higher than the lattice temperature for metals under laser excitation. With the more significant nonthermal effect (increased  $\tau_{e-e}$  and  $\tau_{e-p}$ ) at higher temperature, we would expect a higher A exciton GSB signal, which is consistent with our observation in Figure 3f. The GSB peak blue-shifts with decreasing temperature (Figure S5), further verifying that the GSB signal is from the A exciton of 1L WS<sub>2</sub>.

To understand the ultrafast dynamics of the hot-carrier transferred into WS<sub>2</sub> is fundamentally important and will facilitate the smart design of novel optoelectronic devices. In Figure 4a, the GSB kinetics at the A exciton resonance of Au/WS<sub>2</sub> under 820 nm excitation (blue dots) is compared with that of pristine 1L WS<sub>2</sub> under 420 nm (magenta dots), extracted from Figure 2c and Figure S1, respectively. These experimental results are fitted with a biexponential function (red and black curves). For Au/WS<sub>2</sub> heterojunctions (blue dots, Figure 4a), the increasing time ( $\tau_0$ ) of 160 fs is contributed from both the hot-carrier generation in Au disks and the charge transfer process. After being injected to WS<sub>2</sub>, hot-carrier will undergo a fast decay  $\tau_1$  of 126 fs and a slow decay  $\tau_2$  of 1.90 ps. Apparently, the charge-transfer time scale ( $\sim 160$  fs) is much shorter than  $\tau_{e-e}$  of the sp-band transition ( $\sim 600$  fs), further illustrating that nonthermal electron transfer can compete with e–e scattering before thermalization. However, the  $\tau_{e-e}$  of the d-band transition ( $\sim 90$  fs) is shorter than 160 fs, which suggests that electrons in the d-band transition are thermalized before transfer and agrees with our previous interpretation that nonthermal effects in the d-band is minimal.

For GSB of the A exciton of pristine 1L WS<sub>2</sub> pumped with a 420 nm laser at 5  $\mu\text{J}/\text{cm}^2$  (magenta dots, Figure 4a), a biexponential fitting resolves a fast decay of 1.26 ps and a slow decay of 26.00 ps, respectively. Those two decay channels are assigned to the radiative lifetime of A excitons and the nonradiative exciton–exciton annihilation process, respectively.<sup>59–61</sup> In contrast, the decay dynamics of hot-electrons injected into 1L WS<sub>2</sub> are quite different from the intrinsic photocarriers or excitons. The fast carrier relaxation ( $\tau_1$ ) of hot carriers injected into 1L WS<sub>2</sub> is most likely caused by defect trapping, while the slow carrier relaxation ( $\tau_2$ ) is from radiative recombination at the interface.<sup>39</sup> In addition, the rise time of the exciton population in pristine 1L WS<sub>2</sub> with 420 nm excitation is  $\sim 0.41$  ps contributed by multiple processes including decoherence, carrier thermalization and relaxation, and exciton formation. By contrast, the rise time is around 0.16 ps for the plasmonic-hot-carrier scenario, indicating that plasmonic-hot-carrier-based devices are capable of providing faster response and are promising in many applications such as ultrafast modulators, optical switches, and photodetectors.

Figure 4b shows that hot carriers transferred into WS<sub>2</sub> in the heterojunction area decay faster at elevated temperature. More importantly, the GSB of exciton resonance reaches its maximum more quickly with increasing temperature shown in the inset of Figure 4b, indicating that high temperature can promote a faster hot-carrier transfer. The nonthermal electrons contribute more significantly at elevated temperature as discussed in Figure 3e. As a result, the nonthermal electrons can be injected efficiently into WS<sub>2</sub> before thermalizing. To sum up, the nonthermal electrons can facilitate both an

accelerated hot-carrier injection process and an enhanced efficiency.

## DISCUSSION AND CONCLUSION

We fabricate hybrid samples with exfoliated 1L WS<sub>2</sub> for further justification and indeed observe the same phenomena as discussed above. The optical image and corresponding transmission spectra are shown in Figure S6 with the plasmonic resonance at 830 nm. Figure S7 presents the TA spectra of the Au/exfoliated 1L WS<sub>2</sub> heterojunction under an 830 nm pump, similar to those from the CVD-grown WS<sub>2</sub> and Au heterojunction in Figure 2. After injection into WS<sub>2</sub>, hot electrons undergo a fast decay and a slow decay as well (Figure S7).

In summary, we have studied hot-carrier dynamics of Au/1L WS<sub>2</sub> heterojunction with steady-state and ultrafast optical spectroscopy. When the excitation laser is in resonance with LSPR, hot electrons are generated through the nonradiative inter- and intra-band decay of surface plasmons and can be subsequently injected into WS<sub>2</sub>. We find that the nonthermal hot electrons play a significant role in the charge transfer process and substantially enhance the charge-transfer efficiency at low pump fluence. Temperature-dependent TA spectra reveal that the nonthermal contribution becomes larger with increasing temperature and can accelerate the carrier injection process as well. Finally, the hot carriers injected into 1L WS<sub>2</sub> mainly decay through trap and interface states, which is strikingly different from the intrinsic exciton dynamics of pristine 1L WS<sub>2</sub>. The hot-electron transfer across the metal/semiconductor surface is quite common for a number of semiconducting materials such as CdSe nanorods,<sup>39</sup> TiO<sub>2</sub>,<sup>62</sup> and graphite.<sup>63</sup> Nevertheless, the efficient nonequilibrium hot-electron transfer across the Au/WS<sub>2</sub> interface reported in this work has been overlooked in previous reports. We believe that nonequilibrium hot-electrons may also play an important role in other materials, and our studies can provide some insights for the performance optimization of hot-carrier-based devices. Our results also may serve as guidelines to enhance the hot-electron efficiency by increasing  $\tau_{e-e}$  with other approaches in addition to reducing pump fluence in this work.

## METHODS

**Sample Preparation.** Monolayer WS<sub>2</sub> was grown on a sapphire substrate with a chemical vapor deposition method (or with exfoliation method). After sample growth, a PMMA layer was spin-coated on the sapphire substrate with the thickness of about 200 nm, and an additional E-spacer layer was spin-coated on top of PMMA to make the substrate conductive. The disk array pattern was created on WS<sub>2</sub> directly with a scanning electron microscope (JEOL 7001F) equipped with the nanometer pattern generation system (NPGS). After patterning, the E-spacer layer was removed with water, and the sample was then developed in MIBK:IPA (1:3) solvent for 90 s. After developing, an Au film with thickness of 30 nm was deposited with a thermal evaporator. The sample was ready after the lift-off procedure in acetone.

**Optical Measurement.** (1) The static absorption was measured on a commercial microspectrophotometer (Craic 20). It is capable of measuring the smallest size down to 7  $\mu\text{m}$ , and the wavelength can cover from 300 to 2100 nm. (2) Transient absorption was measured on an ultrafast system (HELIOS). The pump laser with 100 fs time duration and 1

kHz repetition rate is generated by TOPAS pumped by a Spectra Physics Spitfire Ace Ti:sapphire regenerative amplifier, the wavelength is available from 189 to 2000 nm, and the beam diameter is around 100  $\mu\text{m}$ . The probe light is generated from a GaF<sub>2</sub> crystal with the wavelength range from 400 to 800 nm and the beam diameter is around 50  $\mu\text{m}$ .

## ■ ASSOCIATED CONTENT

### SI Supporting Information

The Supporting Information is available free of charge at <https://pubs.acs.org/doi/10.1021/acsp Photonics.1c01938>.

(Figure S1) TA of pristine 1L WS<sub>2</sub>; (Figure S2) Schematic of hot-electron transfer; (Figure S3) Steady PL of Au/1L WS<sub>2</sub> of 820 nm excitation; (Figure S4 and S5) Pump fluence and temperature dependent A exciton bleaching wavelength; (Figure S6 and S7) Hot-electron injection of Au/1L WS<sub>2</sub> sample made with exfoliation method; (Note 1) Pump fluence dependent hot-carrier injection with two-temperature model (PDF)

## ■ AUTHOR INFORMATION

### Corresponding Authors

**Xinglin Wen** – School of Optical and Electronic Information, Wuhan National Laboratory for Optoelectronics, Huazhong University of Science and Technology, Wuhan 430074, China; [orcid.org/0000-0002-8390-4456](https://orcid.org/0000-0002-8390-4456); Email: [wenxl@hust.edu.cn](mailto:wenxl@hust.edu.cn)

**Wei Du** – Institute of Functional Nano & Soft Materials (FUNSOM), Jiangsu Key Laboratory for Carbon-Based Functional Materials & Devices, Soochow University, Suzhou 215123 Jiangsu, China; [orcid.org/0000-0001-8678-8844](https://orcid.org/0000-0001-8678-8844); Email: [duwei2021@suda.edu.cn](mailto:duwei2021@suda.edu.cn)

**Weijie Zhao** – School of Physics, Frontiers Science Center for Mobile Information Communication and Security, Southeast University, Nanjing 211189, China; Purple Mountain Laboratories, Nanjing 211111, China; [orcid.org/0000-0001-6597-7865](https://orcid.org/0000-0001-6597-7865); Email: [zhaowj@seu.edu.cn](mailto:zhaowj@seu.edu.cn)

### Authors

**Sijie Chen** – School of Optical and Electronic Information, Wuhan National Laboratory for Optoelectronics, Huazhong University of Science and Technology, Wuhan 430074, China

**Jiaxin Zhao** – Division of Physics and Applied Physics, School of Physical and Mathematical Sciences, Nanyang Technological University, 637371, Singapore

Complete contact information is available at: <https://pubs.acs.org/doi/10.1021/acsp Photonics.1c01938>

### Funding

X.W. acknowledges the support from NSFC (62005091), Hubei Provincial Natural Science Foundation of China (2020CFB194), and HUST grant (2019kfyXJJS046). W.D. acknowledges the support from Suzhou Key Laboratory of Functional Nano & Soft Materials, Collaborative Innovation Center of Suzhou Nano Science & Technology, the 111 Project, Joint International Research Laboratory of Carbon-Based Functional Materials and Devices. W. Z. is supported by the Fundamental Research Funds for the Central Universities (Grant No. 2242022R10008).

### Notes

The authors declare no competing financial interest.

## ■ REFERENCES

- (1) Hutter, E.; Fendler, J. H. Exploitation of localized surface plasmon resonance. *Adv. Mater.* **2004**, *16*, 1685–1706.
- (2) Willets, K. A.; Van Duyne, R. P. Localized surface plasmon resonance spectroscopy and sensing. *Annu. Rev. Phys. Chem.* **2007**, *58*, 267–297.
- (3) Mayer, K. M.; Hafner, J. H. Localized Surface Plasmon Resonance Sensors. *Chem. Rev.* **2011**, *111*, 3828–3857.
- (4) Nie, S.; Emory, S. R. Probing single molecules and single nanoparticles by surface-enhanced Raman scattering. *Science* **1997**, *275*, 1102–1106.
- (5) Stiles, P. L.; Dieringer, J. A.; Shah, N. C.; et al. Surface-Enhanced Raman Spectroscopy. *Annu. Rev. Anal. Chem.* **2008**, *1*, 601–626.
- (6) Cao, C.; Zhang, J.; Wen, X. L.; et al. Metamaterials-Based Label-Free Nanosensor for Conformation and Affinity Biosensing. *ACS Nano* **2013**, *7*, 7583–7591.
- (7) Le, F.; Brandl, D. W.; Urzhumov, Y. A.; et al. Metallic nanoparticle arrays: A common substrate for both surface-enhanced Raman scattering and surface-enhanced infrared absorption. *ACS Nano* **2008**, *2*, 707–718.
- (8) Kundu, J.; Le, F.; Nordlander, P.; et al. Surface enhanced infrared absorption (SEIRA) spectroscopy on nanoshell aggregate substrates. *Chem. Phys. Lett.* **2008**, *452*, 115–119.
- (9) Oulton, R. F.; Sorger, V. J.; Zentgraf, T.; et al. Plasmon lasers at deep subwavelength scale. *Nature* **2009**, *461*, 629–632.
- (10) Suh, J. Y.; Kim, C. H.; Zhou, W.; et al. Plasmonic Bowtie Nanolaser Arrays. *Nano Lett.* **2012**, *12*, 5769–5774.
- (11) Zhang, Q.; Li, G. Y.; Liu, X. F.; et al. A room temperature low-threshold ultraviolet plasmonic nanolaser. *Nat. Commun.* **2014**, *5*, 4953.
- (12) Kleemann, M. E.; Chikkaraddy, R.; Alexeev, E. M.; et al. Strong-coupling of WSe<sub>2</sub> in ultra-compact plasmonic nanocavities at room temperature. *Nat. Commun.* **2017**, *8*, 1296.
- (13) Chikkaraddy, R.; de Nijs, B.; Benz, F.; et al. Single-molecule strong coupling at room temperature in plasmonic nanocavities. *Nature* **2016**, *535*, 127–130.
- (14) Lundt, N.; Klemmt, S.; Cherotchenko, E.; et al. Room-temperature Tamm-plasmon exciton-polaritons with a WSe<sub>2</sub> monolayer. *Nat. Commun.* **2016**, *7*, 13328.
- (15) Du, W.; Zhao, J. X.; Zhao, W. J.; et al. Ultrafast Modulation of Exciton-Plasmon Coupling in a Monolayer WS<sub>2</sub>-Ag Nanodisk Hybrid System. *ACS Photonics* **2019**, *6*, 2832–2840.
- (16) Brongersma, M. L.; Halas, N. J.; Nordlander, P. Plasmon-induced hot carrier science and technology. *Nat. Nanotechnol.* **2015**, *10*, 25–34.
- (17) Liu, J. G.; Zhang, H.; Link, S.; et al. Relaxation of Plasmon-Induced Hot Carriers. *ACS Photonics* **2018**, *5*, 2584–2595.
- (18) Brown, A. M.; Sundararaman, R.; Narang, P.; et al. Experimental and Ab Initio Ultrafast Carrier Dynamics in Plasmonic Nanoparticles. *Phys. Rev. Lett.* **2017**, *118*, 087401.
- (19) Brown, A. M.; Sundararaman, R.; Narang, P.; et al. Non-radiative Plasmon Decay and Hot Carrier Dynamics: Effects of Phonons, Surfaces, and Geometry. *ACS Nano* **2016**, *10*, 957–966.
- (20) Manjavacas, A.; Liu, J. G.; Kulkarni, V.; et al. Plasmon-Induced Hot Carriers in Metallic Nanoparticles. *ACS Nano* **2014**, *8*, 7630–7638.
- (21) Ng, C.; Cadusch, J. J.; Dligatch, S.; et al. Hot Carrier Extraction with Plasmonic Broadband Absorbers. *ACS Nano* **2016**, *10*, 4704–4711.
- (22) Fang, Z.; Liu, Z.; Wang, Y.; et al. Graphene-antenna sandwich photodetector. *Nano Lett.* **2012**, *12*, 3808–3813.
- (23) Wu, K.; Rodriguez-Cordoba, W. E.; Yang, Y.; et al. Plasmon-induced hot electron transfer from the Au tip to CdS rod in Au nanoheterostructures. *Nano Lett.* **2013**, *13*, 5255–5263.
- (24) Zheng, B. Y.; Zhao, H.; Manjavacas, A.; et al. Distinguishing between plasmon-induced and photoexcited carriers in a device geometry. *Nat. Commun.* **2015**, *6*, 7797.
- (25) Tan, S.; Argondizzo, A.; Ren, J.; et al. Plasmonic coupling at a metal/semiconductor interface. *Nat. Photonics* **2017**, *11*, 806–812.



- (26) Mukherjee, S.; Libisch, F.; Large, N.; et al. Hot electrons do the impossible: plasmon-induced dissociation of H<sub>2</sub> on Au. *Nano Lett.* **2013**, *13*, 240–247.
- (27) Zhou, L. A.; Swearer, D. F.; Zhang, C.; et al. Quantifying hot carrier and thermal contributions in plasmonic photocatalysis. *Science* **2018**, *362*, 69–72.
- (28) Feng, B.; Zhu, J.; Lu, B.; et al. Achieving Infrared Detection by All-Si Plasmonic Hot-Electron Detectors with High Detectivity. *ACS Nano* **2019**, *13*, 8433–8441.
- (29) Wang, W.; Klots, A.; Prasai, D.; et al. Hot Electron-Based Near-Infrared Photodetection Using Bilayer MoS<sub>2</sub>. *Nano Lett.* **2015**, *15*, 7440–7444.
- (30) Knight, M. W.; Sobhani, H.; Nordlander, P.; et al. Photo-detection with Active Optical Antennas. *Science* **2011**, *332*, 702–704.
- (31) Yu, Y.; Ji, Z.; Zu, S.; et al. Ultrafast Plasmonic Hot Electron Transfer in Au Nanoantenna/MoS<sub>2</sub> Heterostructures. *Adv. Funct. Mater.* **2016**, *26*, 6394–6401.
- (32) Wen, X. L.; Xu, W. G.; Zhao, W. J.; et al. Plasmonic Hot Carriers-Controlled Second Harmonic Generation in WSe<sub>2</sub> Bilayers. *Nano Lett.* **2018**, *18*, 1686–1692.
- (33) Taghinejad, M.; Taghinejad, H.; Xu, Z.; et al. Hot-Electron-Assisted Femtosecond All-Optical Modulation in Plasmonics. *Adv. Mater.* **2018**, *30*, 1704915.
- (34) Wang, W. Y.; Klots, A.; Prasai, D.; et al. Hot Electron-Based Near-Infrared Photodetection Using Bilayer MoS<sub>2</sub>. *Nano Lett.* **2015**, *15*, 7440–7444.
- (35) Li, W.; Coppens, Z. J.; Besteiro, L. V.; et al. Circularly polarized light detection with hot electrons in chiral plasmonic metamaterials. *Nat. Commun.* **2015**, *6*, 8379.
- (36) Khurgin, J.; Tsai, W.-Y.; Tsai, D. P.; et al. Landau Damping and Limit to Field Confinement and Enhancement in Plasmonic Dimers. *ACS Photonics* **2017**, *4*, 2871–2880.
- (37) Sundararaman, R.; Narang, P.; Jermyn, A. S.; et al. Theoretical predictions for hot-carrier generation from surface plasmon decay. *Nat. Commun.* **2014**, *5*, 5788.
- (38) Kumar, P. V.; Rossi, T. P.; Marti-Dafcik, D.; et al. Plasmon-Induced Direct Hot-Carrier Transfer at Metal-Acceptor Interfaces. *ACS Nano* **2019**, *13*, 3188–3195.
- (39) Wu, K.; Chen, J.; McBride, J. R.; et al. Efficient hot-electron transfer by a plasmon-induced interfacial charge-transfer transition. *Science* **2015**, *349*, 632–635.
- (40) Arbouet, A.; Voisin, C.; Christofilos, D.; et al. Electron-phonon scattering in metal clusters. *Phys. Rev. Lett.* **2003**, *90*, 177401.
- (41) Giri, A.; Gaskins, J. T.; Foley, B. M.; et al. Experimental evidence of excited electron number density and temperature effects on electron-phonon coupling in gold films. *J. Appl. Phys.* **2015**, *117*, 044305.
- (42) Groeneveld, R. H. M.; Sprik, R.; Lagendijk, A. Effect of a nonthermal electron distribution on the electron-phonon energy relaxation process in noble metals. *Phys. Rev. B* **1992**, *45*, No. 5079.
- (43) de la Torre, A.; Kennes, D. M.; Claassen, M.; et al. Colloquium: Nonthermal pathways to ultrafast control in quantum materials. *Rev. Mod. Phys.* **2021**, *93*, 041002.
- (44) Chen, Y. Z.; Li, Y. J.; Zhao, Y. D.; et al. Highly efficient hot electron harvesting from graphene before electron-hole thermalization. *Sci. Adv.* **2019**, *5*, No. eaax9958.
- (45) Zhou, D. M.; Li, X. F.; Zhou, Q. H.; et al. Infrared driven hot electron generation and transfer from non-noble metal plasmonic nanocrystals. *Nat. Commun.* **2020**, *11*, 2944.
- (46) Cong, C. X.; Shang, J. Z.; Wu, X.; et al. Synthesis and Optical Properties of Large-Area Single-Crystalline 2D Semiconductor WS<sub>2</sub> Monolayer from Chemical Vapor Deposition. *Adv. Opt. Mater.* **2014**, *2*, 131–136.
- (47) Zhu, B. R.; Chen, X.; Cui, X. D. Exciton Binding Energy of Monolayer WS<sub>2</sub>. *Sci. Rep.* **2015**, *5*, 9218.
- (48) Hsu, C. W.; Frisenda, R.; Schmidt, R.; et al. Thickness-Dependent Refractive Index of 1L, 2L, and 3L MoS<sub>2</sub>, MoSe<sub>2</sub>, WS<sub>2</sub>, and WSe<sub>2</sub>. *Adv. Opt. Mater.* **2019**, *7*, 1900239.
- (49) Zhou, M.; Zeng, C. J.; Chen, Y. X.; et al. Evolution from the plasmon to exciton state in ligand-protected atomically precise gold nanoparticles. *Nat. Commun.* **2016**, *7*, 13240.
- (50) Hodak, J. H.; Martini, I.; Hartland, G. V. Spectroscopy and dynamics of nanometer-sized noble metal particles. *J. Phys. Chem. B* **1998**, *102*, 6958–6967.
- (51) Del Fatti, N.; Vallee, F.; Flytzanis, C.; et al. Electron dynamics and surface plasmon resonance nonlinearities in metal nanoparticles. *Chem. Phys.* **2000**, *251*, 215–226.
- (52) Tas, G.; Maris, H. Electron diffusion in metals studied by picosecond ultrasonics. *Phys. Rev. B* **1994**, *49*, 15046.
- (53) Mueller, B. Y.; Rethfeld, B. Relaxation dynamics in laser-excited metals under nonequilibrium conditions. *Phys. Rev. B* **2013**, *87*, 035139.
- (54) Tagliabue, G.; DuChene, J. S.; Abdellah, M.; et al. Ultrafast hot-hole injection modifies hot-electron dynamics in Au/p-GaN heterostructures. *Nat. Mater.* **2020**, *19*, 1312–1318.
- (55) Hattori, Y.; Meng, J.; Zheng, K. B.; et al. Phonon-Assisted Hot Carrier Generation in Plasmonic Semiconductor Systems. *Nano Lett.* **2021**, *21*, 1083–1089.
- (56) Hartland, G. V. Optical Studies of Dynamics in Noble Metal Nanostructures. *Chem. Rev.* **2011**, *111*, 3858–3887.
- (57) Hodak, J. H.; Henglein, A.; Hartland, G. V. Electron-phonon coupling dynamics in very small (between 2 and 8 nm diameter) Au nanoparticles. *J. Chem. Phys.* **2000**, *112*, S942–S947.
- (58) Groeneveld, R. H.; Sprik, R.; Lagendijk, A. J. P. R. B. Femtosecond spectroscopy of electron-electron and electron-phonon energy relaxation in Ag and Au. *Phys. Rev. B* **1995**, *51*, 11433.
- (59) Ruppert, C.; Chernikov, A.; Hill, H. M.; et al. The Role of Electronic and Phononic Excitation in the Optical Response of Monolayer WS<sub>2</sub> after Ultrafast Excitation. *Nano Lett.* **2017**, *17*, 644–651.
- (60) Zhao, J. X.; Zhao, W. J.; Du, W.; et al. Dynamics of exciton energy renormalization in monolayer transition metal disulfides. *Nano Res.* **2020**, *13*, 1399–1405.
- (61) Sun, D. Z.; Rao, Y.; Reider, G. A.; et al. Observation of Rapid Exciton-Exciton Annihilation in Monolayer Molybdenum Disulfide. *Nano Lett.* **2014**, *14*, S625–S629.
- (62) Taghinejad, M.; Xu, Z. H.; Lee, K. T.; et al. Transient Second-Order Nonlinear Media: Breaking the Spatial Symmetry in the Time Domain via Hot-Electron Transfer. *Phys. Rev. Lett.* **2020**, *124*, 013901.
- (63) Tan, S. J.; Dai, Y. A.; Zhang, S. M.; et al. Coherent Electron Transfer at the Ag/Graphite Heterojunction Interface. *Phys. Rev. Lett.* **2018**, *120*, 126801.